Electronic Supplementary Material (ESI) for Journal of Materials Chemistry A.

Electronic Supplementary Information

Enhanced charge carrier separation of manganese (II)-doped graphite carbon nitride: formation of N-Mn bonds from redox reactions

Haiping Li,[a] Yuguo Xia,[a] Tingxia Hu,[b] Quanhua Deng,[b] Na Du [b] and Wanguo Hou *[b]

[a] *National Engineering Research Center for Colloidal Materials, Shandong University, Jinan 250100, P. R. China;*

[b] *Key Laboratory of Colloid and Interface Chemistry (Ministry of Education), Shandong University, Jinan 250100, P. R. China.*

*Email: wghou@sdu.edu.cn

S1. Preparation and characterization of samples

$KMnO_4$ (99.5%), urea (99.0%), KCl (99.5%), and $MnCl_2{\cdot}4H_2O$ (99.0%) were purchased from Sinapharm Chemical Reagent Co., Ltd (China). Tert-butyl alcohol (99.5%), sodium oxalate ()99.8%, $K_2Cr_2O_7$ (99.8%), benzoquinone (99.0%), and 5,5'-dimethyl-1-pirroline-N-oxide (DMPO, 97.0%) were bought from Aladdin (China). All the chemicals were used as received. Ultrapure water was used in all the experiments.

The Mn-doped g-C_3N_4 (g-C_3N_4-Mn) was prepared via a simple calcination process. First, 10 g of urea and 0.02 g of $KMnO_4$ were dissolved in 10 mL of H_2O. Then the solution was distilled at 80 °C to remove the water and the obtained solid was dried at 60 °C for 24 h. The completely dried solid was placed in a crucible with a cover and heated at 550 °C for 4 h in N_2 with a heating rate of 5 °C/min. After cooling naturally to the room temperature, the sample was dispersed in water and stirred for 12 h. The final product was obtained after filtration, washing with water and dried at 60 °C for 24 h. Pure g-C_3N_4 was synthesized via a similar process without the addition of $KMnO_4$. For comparison, 0.0094 g of KCl, 0.0250 g of $MnCl_2{\cdot}4H_2O$ and both of them were substituted for $KMnO_4$ to prepare g-C_3N_4-KCl, g-C_3N_4-$MnCl_2$ and g-C_3N_4-KCl-$MnCl_2$, respectively.

Powder X-ray diffraction (XRD) were measured on a Bruker D8 Advance diffractometer (Germany) with Cu Kα radiation (λ = 1.54184 Å). X-ray photoelectron spectroscopy (XPS) was performed on Thermo Scientific Escalab 250Xi spectrometer (UK) with Al Kα radiation. The C 1s peak at 284.8 eV was used to calibrate peak positions. The ultraviolet photoelectron spectroscopy (UPS) spectra were measured with a monochromatic He I light source (21.22 eV) and a VG Scienta R4000 analyzer. A bias of −5 V was applied to observe the secondary electron cut-off edge. Morphology observation was carried out on a Supra55 field emission-scanning electron microscope (SEM, Zeiss, Germany). Contents and spatial distributions of elements were analyzed by an energy dispersive spectrometer (EDS) equipped in the SEM instrument. N_2 sorption isotherms were measured on a Micromeritics ASAP 2460 instrument. Samples were degassed at 120 °C for 6 h before measurement. Fourier-transform infrared (FT-IR) spectra were recorded on a Bruker Tensor 27 spectrophotometer (Germany). UV-vis diffuse reflectance spectra were measured on an Agilent CARY5000 spectrophotometer (USA). Photoluminescence (PL) spectra were measured on a Perkin-Elmer LS-55 fluorescence spectrometer (USA) with excitation wavelengths of 380–420 nm. Fluorescence decay curves were recorded in an Edinburgh Analytical Instruments FLS920 time-resolved spectrofluorometer (UK). The samples were excited at 377.8 nm with a picosecond pulsed diode laser (EPL-375), and monitored at 460 nm. Electron paramagnetic resonance (EPR) spectra were tested on a Bruker A300-1012 spectrometer (Germany) at the room temperature. The electron spin resonance signals of radicals spin-trapped by spin-trap reagent DMPO were also examined on this spectrometer. Solid-state nuclear magnetic resonance spectrometry (AVANCE III 600, Bruker) was used to measure ^{13}C NMR spectra of samples. Mn K-edge X-ray absorption spectra (XAS) were collected at the beamline 1W1B with a Si (111) double-crystal monochromator at the Beijing Synchrotron Radiation Facility (BSRF). XAS data were analyzed using the standard IFEFFIT procedures. Photoelectrochemical test was carried on an electrochemical work station (CHI770C, China) with a standard three-electrode cell in a 0.1 M Na_2SO_4 solution. Saturated calomel electrode (SCE) and Pt wire were used as the reference and counter electrodes, respectively, with an applied bias of 0.5 V (vs. SCE). The working electrodes were prepared by coating sample slurries onto clean ITO glass, followed by drying for 1 h at 200 °C. The slurries were obtained by grinding the mixture of 0.02 g of samples, 40 μL of PEDOT-PSS and 400 μL of H_2O. A 300-W xenon lamp with a cut-off filter ($\lambda \geq 420$ nm) (Ceaulight, China) were used as the light source.

Photocatalytic performance of the photocatalysts was evaluated via degradation of Rhodamine

B and methyl orange on a XPA-7 photocatalytic reaction apparatus (Xujiang Electromechanical Plant, China).[1] A 500-W xenon lamp equipped with an ultraviolet cutoff filter ($\lambda \geq 420$ nm) was used as the light source. For each run, 0.02 g of photocatalyst was added to 50 mL of 10 mg/L RhB solution, 10 mg/L MO solution, or 20 mg/L resorcinol solution. Before irradiation, the suspension was stirred in the dark for 2 h to reach sorption equilibrium. About 4 mL of suspensions were taken out after a given time and filtered through 0.45-μm poly(ether sulfone) syringe filters. The absorbance of filtrates was analyzed by a Hewlett-Packard 8453 UV-vis spectrophotometer (USA) The maximum absorption wavelengths of RhB, MO, and resorcinol here are 554, 464, and 273 nm, respectively.

Density functional theory (DFT) calculations corrected by the on-site Coulomb interaction were performed by using the Vienna Ab-initio Simulation package (VASP).[2] The exchange-correlation interaction is described by generalized gradient approximation (GGA) with the Perdew-Burke-Ernzerhof (PBE) functional.[3] To better describe non-bonding interactions, Grimme's scheme van der Waals correction is utilized.[4] The energy cut-off is set to 500 eV. The Brillouin zone is sampled using a Monkhorst-Pack 5 × 5 × 3 *K*-point grid.[5, 6] For all the calculations, spin polarization was taken into account and the convergence criteria for the electronic and ionic relaxation are 10^{-5} eV and 0.02 eV/Å, respectively.

S2. The redox reaction between urea and $KMnO_4$

$$CO(NH_2)_2 \text{ (urea)} + KMnO_4 \xrightarrow{\Delta} (C_3N_4)\text{-NH-Mn-NH-}(C_3N_4) + K^+ + N_2\uparrow + H_2O\uparrow + NH_3\uparrow$$

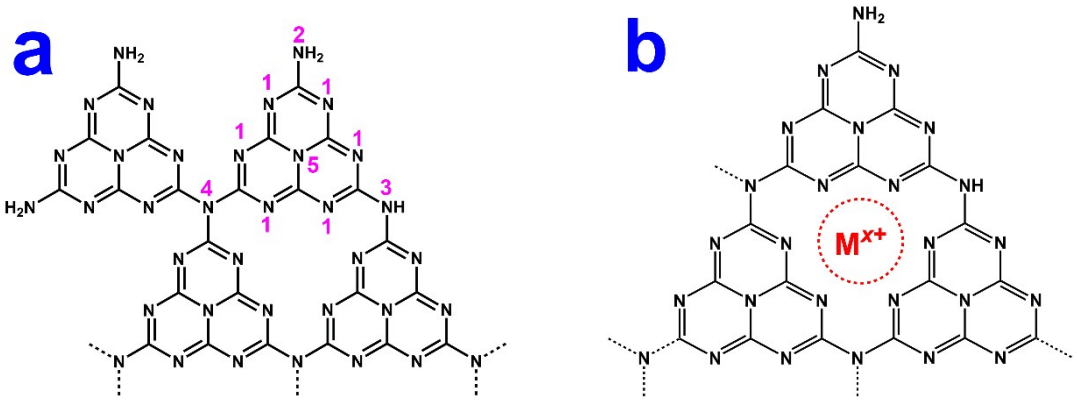

Fig. S1. (a) Possible interacting sites of g-C_3N_4 with metal ions and (b) the interaction of metal ions with N(-C_2). The numbers "1", "2 and 3", and "4 and 5" in (a) mark N(-C_2), N(-H_x), and N(-C_3), respectively.

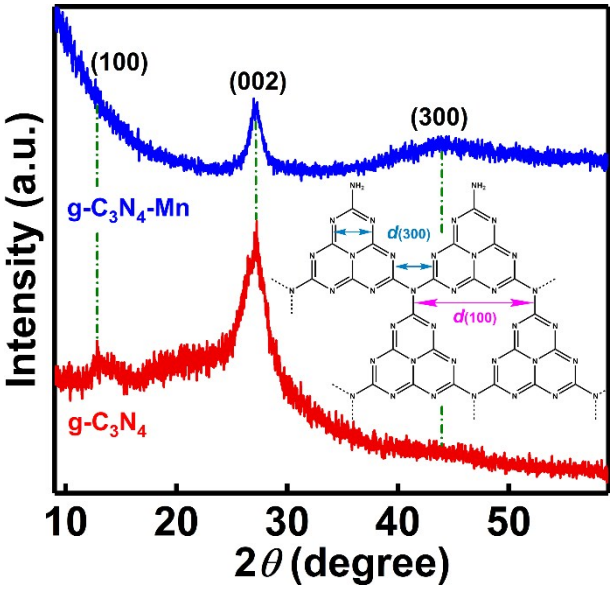

Fig. S2. XRD patterns of the samples. Inset is the structure of g-C_3N_4 with some crystal facet spacings denoted.

In Fig. S2, the X-ray diffraction (XRD) pattern of g-C_3N_4 shows two diffraction peaks at 13.0 and 27.3° which are ascribed to (100) and (002) planes, respectively, and a quite weak peak at ~43.9° corresponding to the (300) plane,[7] indicating successful preparation of the sample. g-C_3N_4-Mn shows similar diffraction peak positions, demonstrating the doping of Mn did not change the basic crystal structure of g-C_3N_4, but weaker (100) and (002) and stronger (300) peaks, suggesting the influence of Mn doping.

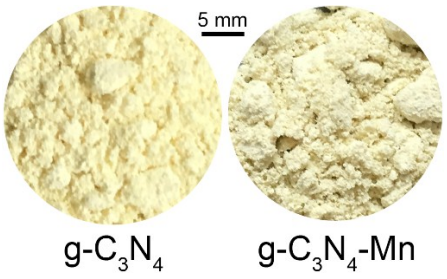

Fig. S3. Color of g-C_3N_4 and g-C_3N_4-Mn samples.

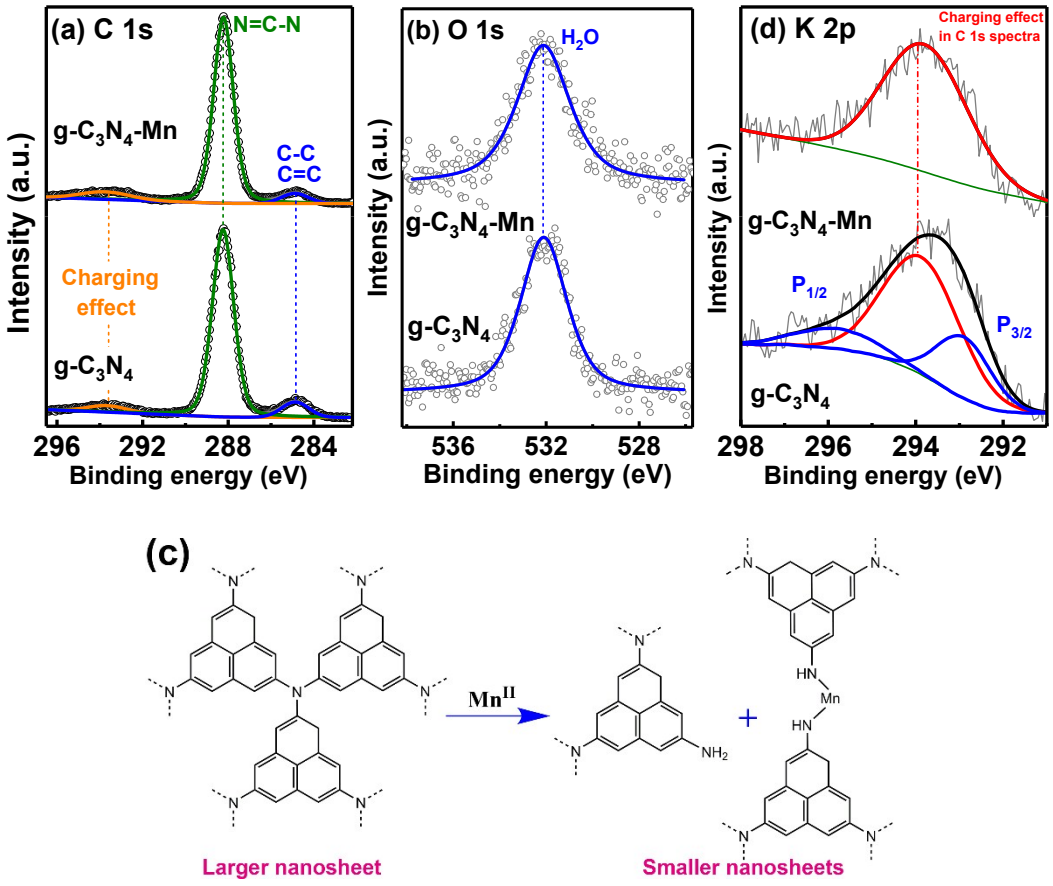

Fig. S4. High-resolution (a) C 1s, (b) O 1s, and (d) K 2p XPS spectra of the samples and (c) the schematic diagram for formation of N_H-Mn^{II} bonds induced decrease in the size of g-C_3N_4-Mn nanosheets.

In Fig. S4a, peaks at binding energy (BE) of 284.8, 288.3, and 293.6 eV for the g-C_3N_4 are ascribed to adventitious carbon,[8] N=C-N bonds, and charging effect of conjugated systems, respectively.[9] In the XPS O 1s core-level spectra of the g-C_3N_4 (Fig. S4b), the peak around BE of 532.1 eV is ascribed to the adsorbed hydroxyl species (e.g. H_2O) on surfaces of the samples. The corresponding peaks of g-C_3N_4-Mn do not show any movement and no new peaks are observed (Fig. S4a and b), suggesting the influence of Mn doping is weak and C-Mn^{II} and O-Mn^{II} bonds were not formed in the g-C_3N_4-Mn. Fig. S4d shows the high-resolution K 2p XPS spectra. Compared with the peak of g-C_3N_4, that of the g-C_3N_4-Mn can be deconvoluted into three peaks, and the peaks around BE of 293.1 and 295.9 eV correspond to $2P_{3/2}$ and $2P_{1/2}$ of K^+, respectively.[10, 11]

Table S1. Physicochemical properties of g-C_3N_4 and g-C_3N_4-Mn.

Sample	S_{BET} [a] (m^2g^{-1})	Pore volume (cm^3g^{-1})	E_g [b] (eV)	$R_{N/C}$ [c]	W_{Mn} [d] (wt%)	W_K [e] (wt%)
g-C_3N_4	34.8	1.033	2.73	1.31/1	0	0
g-C_3N_4-Mn	99.3	1.045	2.70	1.29/1	~3.9	~1.4

[a] BET specific surface area; [b] Energy band gap; [c] Molar ratio of N/C from XPS data; [d] Content of Mn; [e] Content of K.

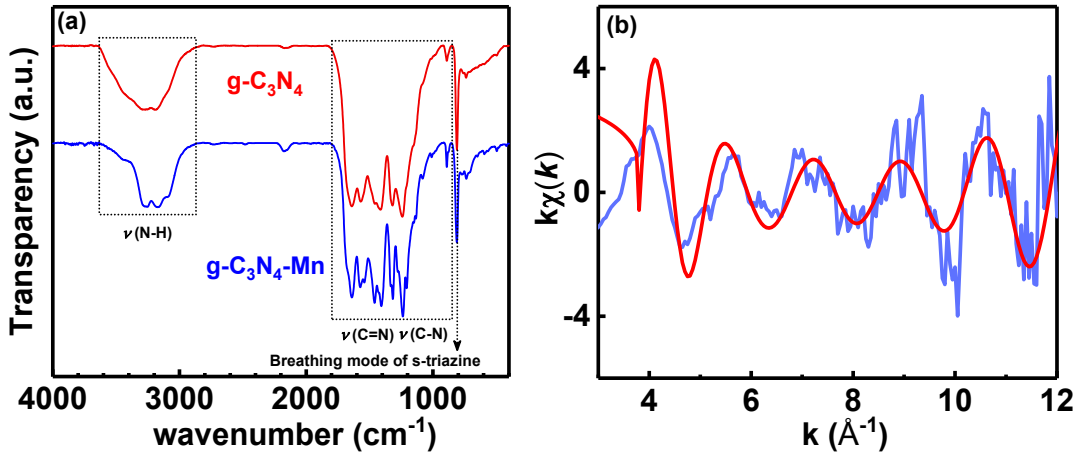

Fig. S5. (a) FT-IR spectra of g-C_3N_4 and g-C_3N_4-Mn and (a) Mn K-edge EXAFS oscillation function $k^2\chi(k)$ spectra for g-C_3N_4-Mn. The red line in (b) is the Mn-N single-shell fitting result.

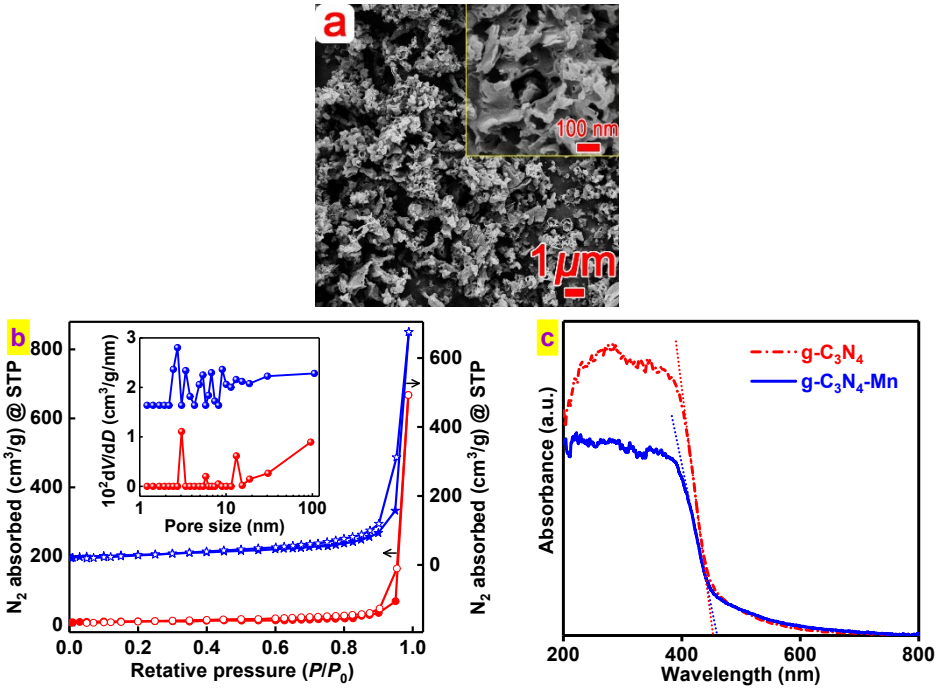

Fig. S6. (a) The SEM image of pure g-C_3N_4, (b) N_2 adsorption-desorption isotherms, (Inset in b) pore size distribution curves obtained via calculating the adsorption-branch data of isotherms using a Barrett-Joyner-Halenda (BJH) method, and (c) UV-vis diffuse reflectance spectra of g-C_3N_4 and g-C_3N_4-Mn.

N_2 sorption isotherms were measured to characterize the specific surface areas and porous structures of the samples (Fig. S6b). Both the g-C_3N_4 and the g-C_3N_4-Mn show a typical type IV isotherm with a pronounced type H3 hysteresis loop, indicating the formation of slit-like pores via aggregation of nanosheets.[12] The BET surface area of the g-C_3N_4-Mn (99.3 m^2/g) is ~3 times that of the g-C_3N_4-Mn (34.8 m^2/g) (Table S1). Pore size (D) distribution curves (Inset in Fig. S6b) of them reveal that the g-C_3N_4-Mn possesses much denser pore size distribution (2.7, 3.4, 5.4, 6.8, 9.0 and 13.1 nm) and wider distribution range than the g-C_3N_4 (3.1, 5.8 and 13.1 nm) at D < ~20 nm, demonstrating that the former contains much more pores. Photoabsorption properties of the

samples are shown in UV-Vis diffuse reflectance spectra (Fig. S6c). The g-C_3N_4-Mn exhibits a little higher photoabsorption than the g-C_3N_4 at λ > ~490 nm. Dotted lines in the Fig. S6c denote the absorption edges (λ_e) of g-C_3N_4 and g-C_3N_4-Mn are 454 and 459 nm, corresponding to the energy band gaps (E_g) of 2.73 and 2.70 eV (1240/λ_e)[13], respectively (Table S1).

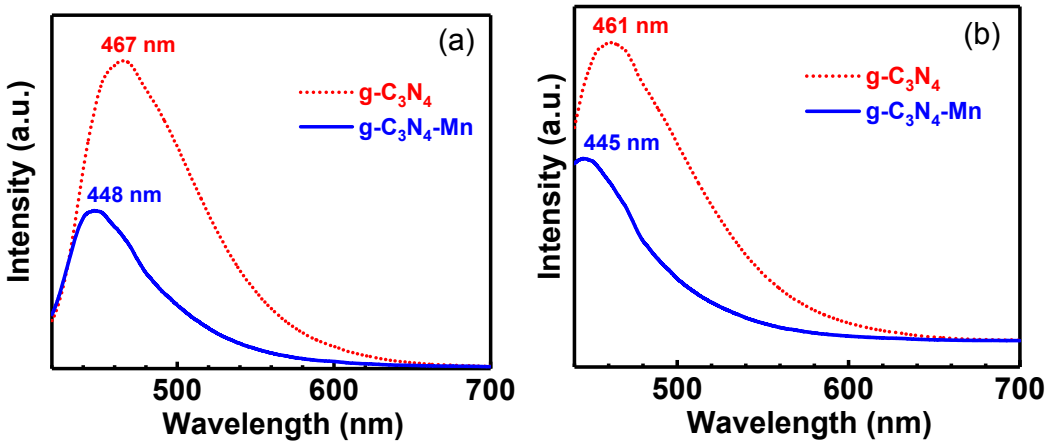

Fig. S7. PL spectra of samples excited at (a) 400 nm and (b) 420 nm.

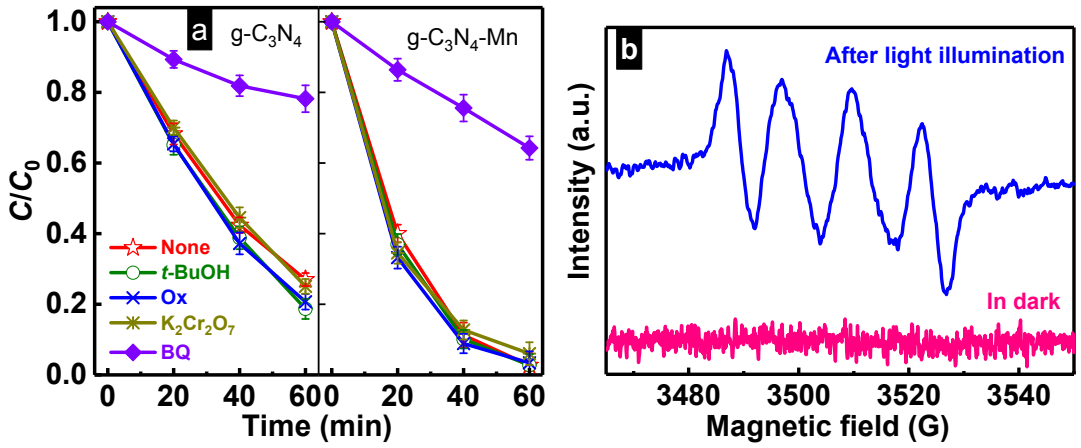

Fig. S8. (a) Photocatalytic degradation of RhB on the samples in the presence of different scavengers: 20 mM tert-butyl alcohol (*t*-BuOH), 0.2 mM sodium oxalate (Ox), 10 mM $K_2Cr_2O_7$, and 0.1 mM benzoquinone (BQ); and (b) ESR spectra of DMPO-•O^{2-} for g-C_3N_4-Mn in dark and after light irradiation for 10 min. DMPO is used as the radical trapper and a 300-W Xe lamp as the light source.

As shown in Fig. S8a, tert-butyl alcohol, sodium oxalate, $K_2Cr_2O_7$, and benzoquinone were used to detect hydroxyl radicals, holes, free electrons and superoxide radicals, respectively.[9] When adding tert-butyl alcohol, sodium oxalate and $K_2Cr_2O_7$ to the g-C_3N_4 or g-C_3N_4-Mn suspension, no obvious decrease in the photoactivity was observed, but the addition of benzoquinone considerably decreases the photoactivity of both the g-C_3N_4 and the g-C_3N_4-Mn, suggesting superoxide radicals are the major reactive oxygen species in the photodegradation reaction. The ESR spectrum of DMPO-•O^{2-} for the g-C_3N_4-Mn shows no peaks in dark and typical four peaks after light irradiation for 10 min (Fig. S8b), further demonstrating the formation of •O^{2-} in the photoreactive process.[14, 15]

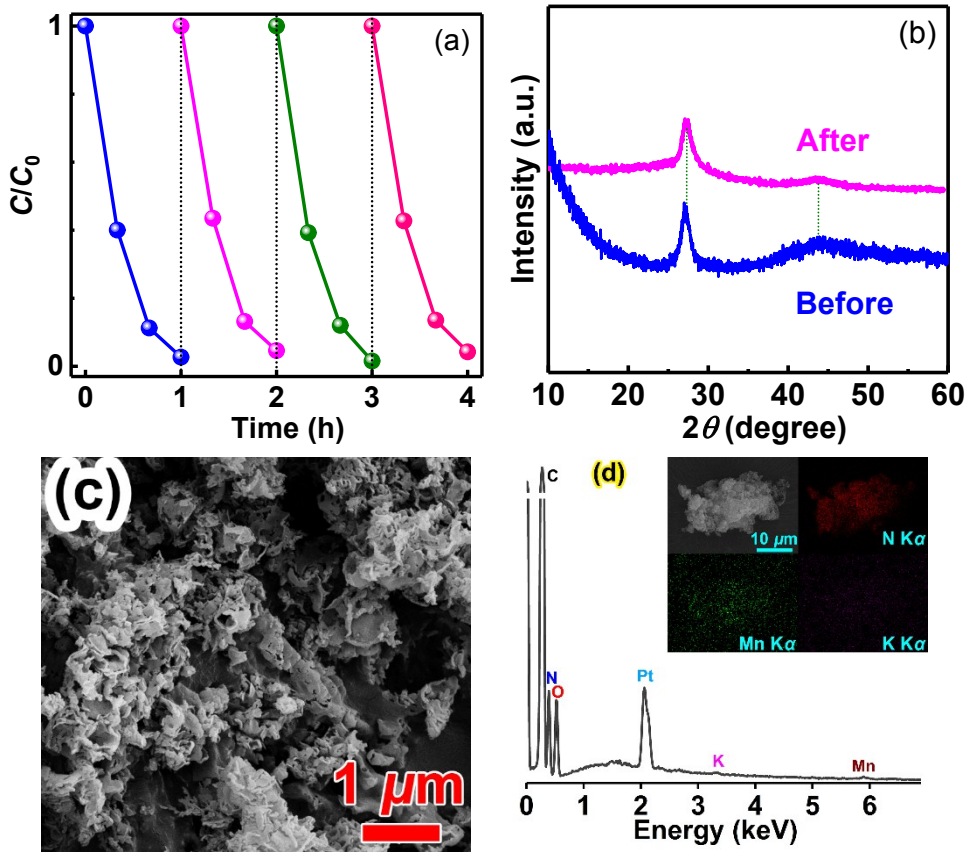

Fig. S9. (a) Cyclic experiments for photodegradation of RhB on g-C_3N_4-Mn; (b) XRD patterns of g-C_3N_4-Mn before and after the cyclic experiments; and (c) SEM and (d) EDS images of the g-C_3N_4-Mn after the cyclic experiments. Pt in (d) was sprayed to increase conductivity of the sample.

As shown in Fig. S9a, after four continuous runs of RhB photodegradation on g-C_3N_4-Mn, there is no obvious decrease in the efficiency. The XRD pattern and the SEM image of the g-C_3N_4-Mn after the cyclic experiments (Fig. S9b and c) are similar to those before the cyclic experiments (Fig. 2). The EDS results of the sample after the cyclic experiments (Fig. S9d) also show the existence Mn. These indicate a good chemical stability of the sample.

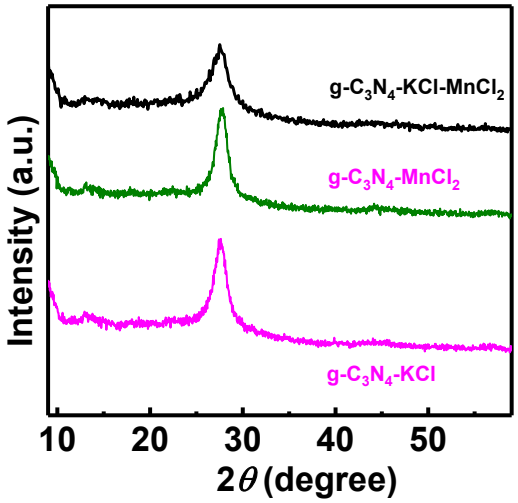

Fig. S10. XRD patterns of different samples.

In Fig. S10, all the peaks of the g-C_3N_4 samples match well with reported XRD results of g-C_3N_4,[5, 12, 13] indicating the successful preparation of samples.

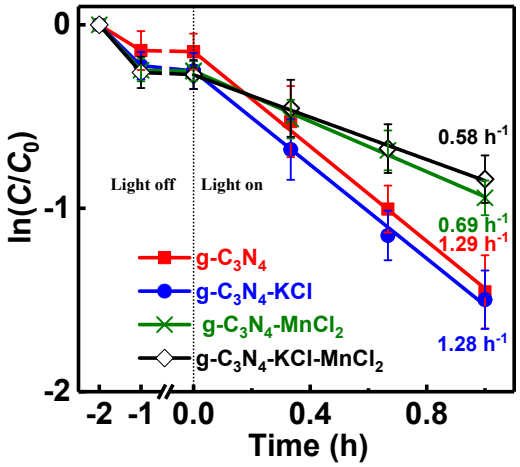

Fig. S11. Photocatalytic degradation of RhB on various photocatalysts under visible light irradiation.

To exclude the influence of remaining K ions in the g-C_3N_4-Mn on the photoactivity, the photoactivity of g-C_3N_4-KCl (see S1 and Fig. S10) was tested in photodegradation of RhB (Fig. S11). The g-C_3N_4-KCl possesses a similar *k* value as pure g-C_3N_4, meaning a negligible influence of the remaining K ions. Actually, the doping amount of K ions must be very high to improves the photoactivity of g-C_3N_4.[10] To compare the influence of Mn doping ways on the photoactivity of the g-C_3N_4-Mn and exclude the synergism of Mn and K, $MnCl_2$ and the mixture of KCl and $MnCl_2$ was substituted for $KMnO_4$ to dope g-C_3N_4, to obtain g-C_3N_4-$MnCl_2$ and g-C_3N_4-KCl-$MnCl_2$, respectively (Fig. S10). The g-C_3N_4-$MnCl_2$ and the g-C_3N_4-KCl-$MnCl_2$ exhibit lower RhB photodegradation efficiencies than pure g-C_3N_4 (Fig. S11), demonstrating that the MnO_4^- is a more effective doping agent than the low valent Mn^{2+}, and that there is no synergism between Mn and K.

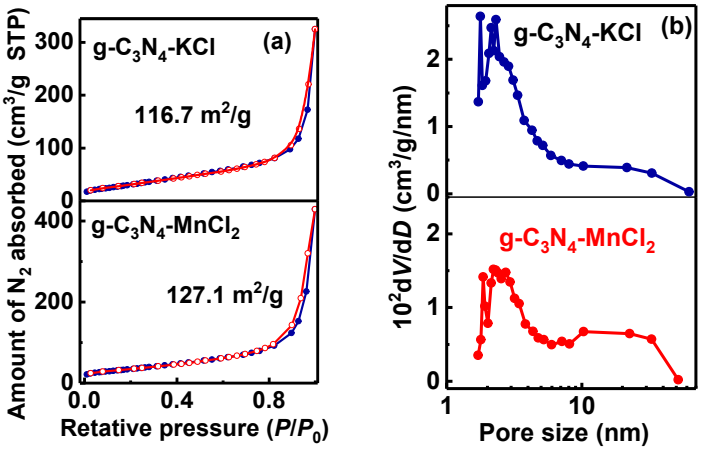

Fig. S12. (a) N_2 adsorption-desorption isotherms and (b) pore size distribution curves obtained via calculating the adsorption-branch data of isotherms using a Barrett-Joyner-Halenda (BJH) method, for different samples. Numbers in (a) are BET specific surface areas.

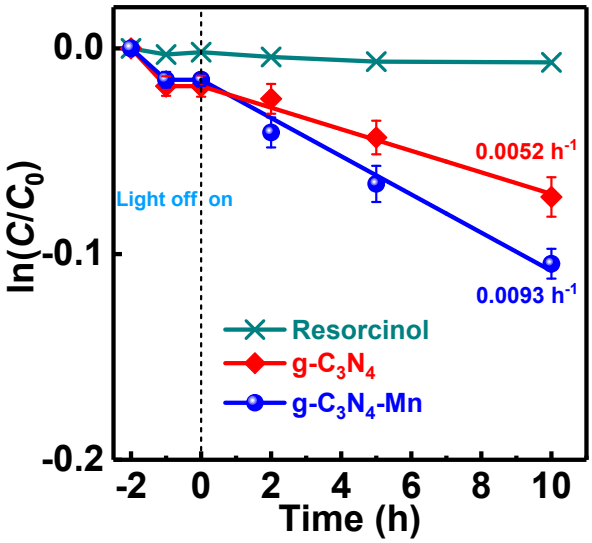

Fig. S13. Photocatalytic degradation of resorcinol on different samples under visible light irradiation ($\lambda \geq 420$ nm). Straight lines in the "Light on" parts were obtained by fitting the data to a pseudo-first-order kinetic model, $-\ln(C/C_0) = kt$ where k, t, C_0, and C are the rate constant, the reaction time, the initial organic concenration, and the organic concentration at t, respectively, and numbers are corresponding rate constants.

References

1 H. Li, Q. Deng, J. Liu, W. Hou, N. Du, R. Zhang and X. Tao, *Catal. Sci. Technol.*, 2014, **4**, 1028-1037.

2 G. Kresse and J. Furthmüller, *Phys. Rev. B*, 1996, **54**, 11169-11186.

3 J. P. Perdew, K. Burke and M. Ernzerhof, *Phys. Rev. Lett.*, 1996, **77**, 3865-3868.

4 S. Grimme, J. Antony, S. Ehrlich and H. Krieg, *J. Chem. Phys.*, 2010, **132**, 154104.

5 Y. Zheng, L. Lin, B. Wang and X. Wang, *Angew. Chem. Int. Ed.*, 2015, **54**, 12868-12884.

6 T. Xiong, W. Cen, Y. Zhang and F. Dong, *ACS Catal.*, 2016, **6**, 2462-2472.
7 F. Fina, S. K. Callear, G. M. Carins and J. T. S. Irvine, *Chem. Mater.*, 2015, **27**, 2612-2618.
8 C. Han, L. Wu, L. Ge, Y. Li and Z. Zhao, *Carbon*, 2015, **92**, 31-40.
9 H. Li, J. Liu, W. Hou, N. Du, R. Zhang and X. Tao, *Appl. Catal. B*, 2014, **160-161**, 89-97.
10 M. Wu, J. M. Yan, X. N. Tang, M. Zhao and Q. Jiang, *ChemSusChem*, 2014, **7**, 2654-2658.
11 M. Zhang, X. Bai, D. Liu, J. Wang and Y. Zhu, *Appl. Catal. B*, 2015, **164**, 77-81.
12 L. Lin, H. Ou, Y. Zhang and X. Wang, *ACS Catal.*, 2016, **6**, 3921-3931.
13 S. Cao, J. Low, J. Yu and M. Jaroniec, *Adv. Mater.*, 2015, **27**, 2150-2176.
14 S. Wang, X. Ding, X. Zhang, H. Pang, X. Hai, G. Zhan, W. Zhou, H. Song, L. Zhang, H. Chen and J. Ye, *Adv. Funct. Mater.*, 2017, **27**, 1703923.
15 W. Zou, L. Zhang, L. Liu, X. Wang, J. Sun, S. Wu, Y. Deng, C. Tang, F. Gao and L. Dong, *Appl. Catal. B*, 2016, **181**, 495-503.